Crystallization-Driven Flows within Evaporating Aqueous Saline Droplets

Crystallisation-driven Flows within Evaporating Aqueous Saline Droplets

Marina Efstratiou[*1], John Christy[1], and Khellil Sefiane[1, 2]*

1. Institute of Mutliscale Thermofluids, School of Engineering, The University of Edinburgh, King's Buildings, Mayfield Road, Edinburgh EH9 3FD, United Kingdom

2. Tianjin Key Lab of Refrigeration Technology, Tianjin University of Commerce, Tianjin City 300134, PR China

KEYWORDS. Aqueous saline drops, salt, sodium chloride, evaporation, flow, micro –PIV, solutal Marangoni, convection, continuity, crystallisation

ABSTRACT

Using micro-PIV (Particle Image Velocimetry), we observe for the first time, the direct correlation between crystallisation and hydrodynamics in evaporating micro-litre saline (1M NaCl) sessile drops. The relationship is demonstrated by a remarkable jet of liquid along the base of the drops, induced by and directed at the point of nucleation and subsequent crystal growth. Prior to

nucleation the flow is more uniformly outward with the magnitude of the velocity decreasing with time. From calculations and the flow measurements in the two observed stages of evaporation (prior to nucleation and during crystallisation), this jet can be explained on the basis of competition between solutal Marangoni convection and mass-conservation flow. The jet of fluid leads to vortices on either side of the crystal in which the salt concentration is reduced, providing a potential explanation as to why NaCl deposits as a sequence of discrete crystals rather than as a continuous ring for such drops.

INTRODUCTION

Following Deegan's paper[1] explaining how the 'coffee ring' effect arises in the drying of drops containing suspensions or soluble solids, there has been increased interest in the study of sessile drops of both pure[2,3] and complex fluids[4–10] and of the patterns arising from drop evaporation[11–13]. Recently, interest has moved towards the drying of saline drops in relation to weathering processes, pharmaceutical applications and medical diagnostics. For saline droplets, some papers report studies on the patterns arising from full desiccation of the drops, whilst others report on the influence of concentration gradients on the drying process[4,14–21]. However, no publication has as yet studied what happens to internally induced flows during nucleation and crystallisation. In this paper, we demonstrate work conducted to discover why on evaporation, for micro-litre drops of relatively concentrated saline solution, instead of obtaining a complete crystal ring towards the outer edge of the drop, a ring of roughly evenly spaced crystals is observed.

The effect of various salts on the evaporation rate and on the contact line dynamics has been studied for a variety of drop sizes. Sghaier (2006) noted that the contact angle increases with increasing concentration of NaCl in aqueous drops on glass slides of various wettability, proposing

an equation for equilibrium contact angle as a function of concentration [21]. Zhong (2017) noted that for saline solutions on silicon and PMMA, the contact angle rises during evaporation, with the contact line sliding, whereas on glass the contact line is pinned [22]. The evaporation rate is observed to decrease in the course of evaporation on heated surfaces due to the residual salt (NaCl, $CaCl_2$, LiCl, LiBr) concentration increasing and thus lowering the saturated vapour pressure [4,16,23,24].

Kang (2013) and Soulie (2015) reported on the development of a toroidal vortex due to an outward concentration-driven Marangoni convection along the air-liquid interface from particle streak methods[25,26]. Marin (2019) has recently observed how this flow leads to suspended particles being carried to the contact line along the air interface to form a ring stain at the contact line, similar to that observed by Deegan, but with Marangoni convection being the driving mechanism[27].

Various researchers have investigated the patterns formed when saline droplets evaporate[11,28–30]. Due to the disparity in droplet size, wettability of solid substrate, specific salts studied and initial salt concentration, direct comparison between patterns is not readily possible. However, in general, for hydrophilic surfaces crystallisation occurs close to the initial three-phase contact line with additional rings if the contact line recedes during evaporation. For high initial salt concentration, discrete crystals may be found either in the centre of the drop or in a ring near the original contact line. Desarnaud (2014) has investigated the nucleation of NaCl crystallisation from supersaturated solutions, noting that in all cases nucleation commences at approximately 160% of the saturation concentration, leading to very rapid crystal growth[31]. Vazquez (2015), using IR thermography, has shown that the temperature distribution of an evaporating saline drop remains almost isothermal during most of the evaporation, except during the latter stages when almost all of the water has evaporated[18]. Zhang (2015) conducted a molecular dynamics simulation of nano-

droplets to explain the increase in contact angle with salt concentration. They also predicted that a single crystal would form on hydrophobic surfaces, but that a crystal ring would form on hydrophilic surfaces[19]. However, no experiments have yet been performed observing flows induced due to the crystallisation process itself.

Although sodium chloride has been examined in different applications, other studies have mainly focused on the investigation of the pattern formation arising from drying salt-water droplets on different solid substrates. In particular, the direct impact of crystallisation on flows has not yet been reported on. There are speculations regarding the mechanisms of crystal deposition, nevertheless, no experimental evidence justifies the formation of a ring of spaced crystals around the droplet edge on hydrophilic surfaces. In this paper we report the existence of a crystallisation-driven flow during the evaporation of aqueous saline solution droplets which leads to the formation of a spaced-crystal ring on the periphery of the initial droplet. We investigate the link between the deposit formation and the flows arising in aqueous saline solution micro-litre droplets on hydrophilic glass slides with the use of micro-PIV (Particle Image Velocimetry). We also employ IRT (Infrared Thermography) to elucidate whether the flows occurring are a result of thermal rather than concentration effects.

EXPERIMENTAL SECTION

Materials

Aqueous 1M sodium chloride (S7653, Sigma Aldrich) solutions were prepared for the experiments, using deionized water acquired from a Centra R200 Purification and Distribution System. 1.2 ± 0.2 μL droplets were deposited on hydrophilic glass slides (Breckland Scientific Supplies - initial contact angle: 25^{o}) cleaned in an ultrasonic water bath with distilled, deionized

water for 15 minutes and dried using an air gun prior to the experiments. The thickness of the glass slides was 1-1.2 mm. It is worth noting that the same phenomenon is observed for initial contact angles of up to 40^{o} and for larger droplets that have been examined (2.7 ± 0.5 μL). However, since only a smaller segment of the droplet could be examined for larger droplets, we present here the results for 1.2±0.2 μL where, with appropriate magnification, almost the whole base of the droplet is visible in the images. Due to the use of commercially available glass slides, there was a slight variation (± 5 degrees) between the initial contact angles for the experiments. The experiments were performed under ambient conditions. Both temperature (T=25±1 ^{o}C) and humidity levels (RH: 32-37%) were monitored throughout the experimental procedure. All the experiments were repeated at least three times.

The flow field during the evaporation and crystallisation of salt-water droplets was acquired using a micro-PIV system. The droplets were seeded with 0.05% fluorescent microspheres (1 μm diameter, Nile-red, carboxylate-modified FluoSphere ® beads of density 1.05 g·cm^{3}) (F8819-Invitrogen) for the experiments. Fluorescent particles were used in order to avoid diffractive halos associated with light scattering from particles having a diameter close to that of the wavelength of the light. Trials confirmed that the concentration of the seeding particles did not affect the final crystal patterns and thus the flow within the evaporating droplets. The droplets were observed through the flat base of an inverted microscope (Leica DMI5000 M) to avoid optical distortions caused by the curvature of their upper surface. The thickness of the imaging plane was defined by the depth of field of the microscope (approximately 10 μm for the 5x lens used). A pulsed diode laser (New Wave Pegasus) emitting at 527 nm, was used to cause the particles to fluoresce at 575 nm and an optical filter ensured that laser light did not reach the camera (Dantec Dynamics Nanosense MkIII 1280x1024 pixels). Velocity maps were generated from image pairs for every

0.5 seconds over the lifetime of the droplet and vorticity measurements were extracted from the velocity maps. Images of the final deposition patterns were also acquired with white light after the drying process was completed.

The observation of NaCl crystallisation was also carried out using passive IR thermography, in order to investigate whether the observable flows were generated due to thermal effects. The acquisition system was a FLIR A655sc long wave infrared thermography camera (7.5 – 14 μm) which enables investigation over a temperature range from -40 to 150 ^{o}C and an accuracy of ± 2% (or ± 2 ^{o}C) of the reading. The detector type was an uncooled microbolometre, providing an image resolution of 640 x 480 pixels. The noise signal was approximately 30 mK. The recorded signal depended on the temperature and emissivity. All the images were acquired and analysed using FLIR ResearchIR software. A black adhesive tape was stuck to the glass slide (bottom surface), acting as a reference material. Its emissivity was determined to be 0.95 in the wavelength analysed by the camera.

RESULTS AND DISCUSSION

The droplets spread with a low equilibrium contact angle (25^{o} ± 5^{o}) and the drying process occurred with a constant contact radius for the most part of the droplet's lifetime. The diameter of the droplet was constant up to at least 91-92% of the final desiccation time, when a decrease of approximately 1-2% of the initial diameter was observed. This slight deviation of the diameter from its initial value was caused by crystal growth, however it was considered to be negligible. A ring of crystals formed at approximately evenly spaced intervals in the vicinity of the initial contact line (Figure 1).

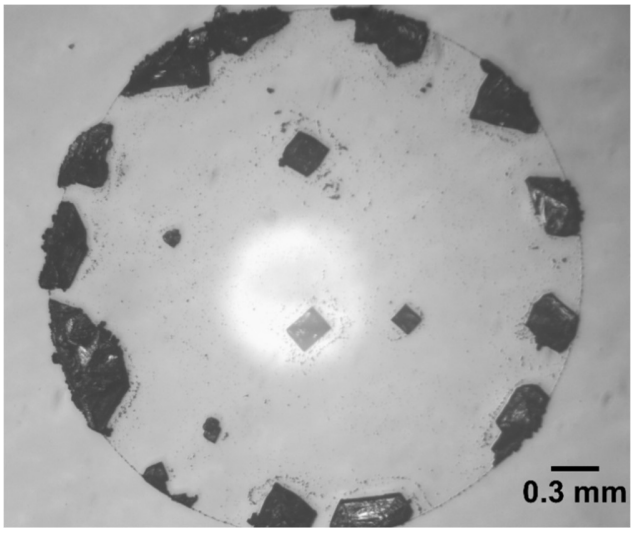

Figure 1: Final crystal ring on the contact line after the evaporation of aqueous saline droplets (1.2 ± 0.2 μL) on hydrophilic glass slides.

Micro-PIV, focussed on a plane approximately 10μm above the substrate, revealed two distinct stages during the evaporation of the saline drops (Figure 2). During the early part of the first stage (I) (up to 60% of the final evaporation time), an initial slow generally-outward flow is observed along the base of the droplet. The flow is not perfectly radially outward because of the effect of solutal Marangoni convection at the droplet surface. During stage I, the outward flow at the base decreases by an order of magnitude immediately prior to the nucleation of the first crystal near the periphery of the droplet. This lasts until ~70% of the final drying time has elapsed. The maximum recorded velocity in this stage is in the order of hundreds of nm/sec. After stage I, a strong, jet-like flow is observed towards the point where the first crystal forms. The flow commences before the crystal is visible and continues as the crystal grows. This jet-like flow leads to the formation of two vortices as it displaces fluid out along the contact line (See Movie SM1 Supporting Information). The maximum velocity in this jet is almost 20 μm/sec. Within a short period, other crystals start to form in other regions on the periphery, each with their own associated jets,

increasing the number of vortices within the droplet (stage II), which suggests that the flow at this stage is driven by the nucleation and growth of crystals.

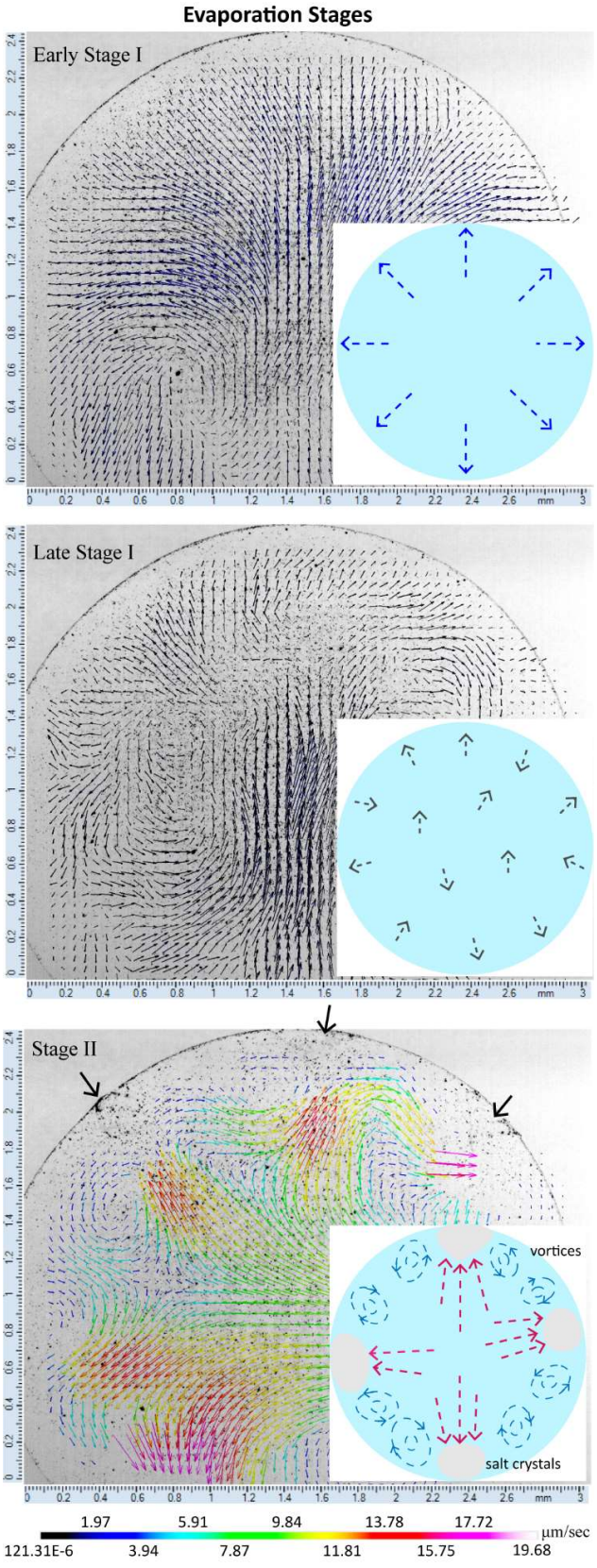
Evaporation Stages
Early Stage I
Late Stage I
Stage II
vortices
salt crystals
1.97
5.91
9.84
13.78
17.72
μm/sec
121.31E-6
3.94
7.87
11.81
15.75
19.68

Figure 2: Micro-PIV velocity vector maps for the different evaporation stages. Early stage I: generally outward flow; Late Stage I: almost stationary; Stage II: strong jet-like flows towards the points of crystal growth and vortex formation within the flow. Insets are schematic diagrams of flow structure.

The graph of base area of the growing crystal versus time (Figure 3) suggests that the jet of fluid commences at the onset of nucleation.

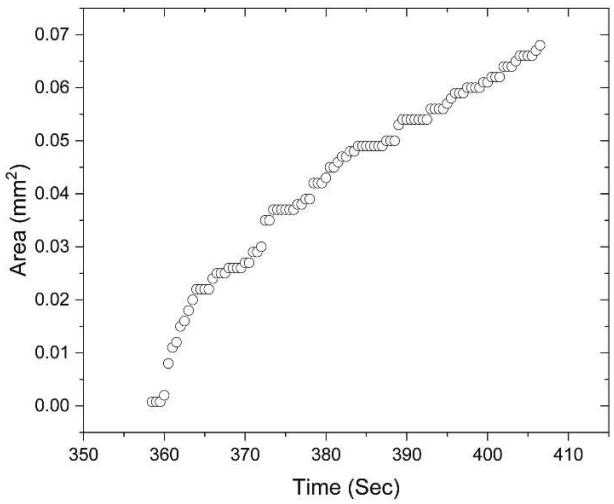

Figure 3: Base area of the growing crystal versus time. Measurements were taken from the moment the crystal was visible within the droplet; ~359 seconds after droplet deposition on the substrate (Time t = 0 seconds is the moment of droplet deposition on the substrate).

We analyse the flow in terms both of capillary flow to account for evaporative flux at the contact line[1] and of Marangoni surface tension-driven flows. For hydrophilic, sessile micro-droplets, water evaporates preferentially near the contact line due to vapour diffusion constraints, increasing the NaCl concentration at the contact line. This generates a concentration gradient and therefore a strong Marangoni flow from the apex of the droplet towards the contact line. The internal flow depends on the relative magnitudes of the Marangoni surface flows and the evaporation rate, with

a toroidal vortex occurring if Marangoni flows exceed the evaporative flux[3,20]. However, where the initial contact angle between the solution and the substrate is low, the evaporative flux tends to exceed the Marangoni flux giving an outward flow throughout the drop, as in our experiments. We estimate the velocities at 75% of the full radius of the drop, since we get the most accurate micro-PIV velocity measurements in that region. Measured velocities for early stage I are ~3 μm/sec at 75% of the radius and 10μm above the base of the drop. The droplet height at the end of this stage, when the contact angle is ~8.5°, is approximately 50 μm as calculated using the spherical cap approximation,

$$h(r,t) = \sqrt{\frac{R^2}{sin^2\theta} - r^2} - \frac{R}{tan\theta} \quad (1)$$

where R is the full radius of the droplet, r is 75% R and θ is the contact angle between the droplet and the substrate (Figure 4). The liquid volumetric flow rate to account for evaporation is 0.002 mm^3/s (experimentally determined). Based on the droplet height at 75% of the radial displacement, the velocity required to supply the evaporative flux is ~6 μm/sec. This is twice the micro-PIV (1-3 μm/sec) measurement, suggesting that there is a solutal Marangoni convection at the surface, arising from the bulk concentration near the apex remaining around 1M whilst that at the contact line rises towards saturation (5.2M) and beyond. For this early stage of evaporation, just over 50% of the volumetric flow required to account for evaporation at the outer edge of the drop appears to arise from surface flows.

Figure 4 shows information about the drying drop at different stages of evaporation, along with schematics illustrating the flows at the air-liquid interface and the base of the droplet.

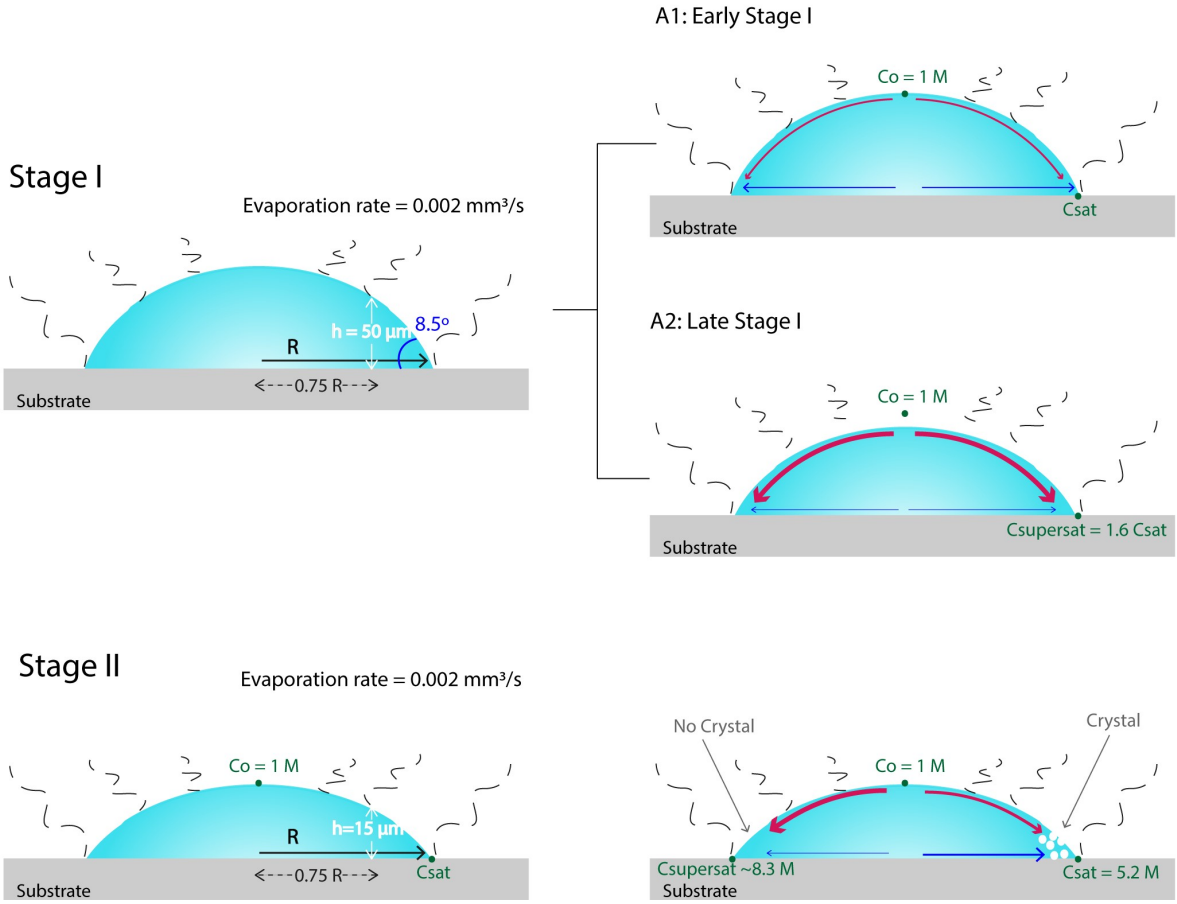

Figure 4: Schematic of the evaporating droplet for stages I and II. The images on the left show the heights of the drying drop at the end of early stage I (onset of late stage I) and the start of stage II. Images on the right show the flows for early Stage I, late Stage I and Stage II from top to bottom. The flow schematic for stage II shows the concentration difference prior to and upon crystal nucleation. The red arrows indicate the convective Marangoni flow at the air-liquid interface, whereas the blue arrows represent the outward flow at the base of the drop. The arrow thickness is representative of the flow magnitude in each stage.

However, later in stage I, just before crystallisation occurs, the velocities near the base of the droplet decrease significantly. We assume that, as the drop is at the point of incipient nucleation near the contact line, the concentration near the contact line is 1.6 times the saturation concentration [34], while that near the apex is still 1M and that the Marangoni-driven convective flow at the air–liquid interface is sufficient to supply almost all of the evaporative flux, causing the flow at the base to decrease to almost zero. From the shear stress equation, the resulting velocity is estimated by

$$v = \frac{1}{\eta}\left(\frac{\partial \gamma}{\partial c}\right)\frac{\Delta c h}{l} \tag{2}$$

where η is the fluid viscosity (~ 0.01 Pa·s), $\frac{\partial \gamma}{\partial c}$ is the change in the surface tension with salt concentration $\left(0.00162\ \frac{\frac{N}{m}}{\frac{mol}{L}}\right)$, Δc is the salt concentration difference along the droplet air-liquid interface, h is the thickness of the film, and l the film width. We have estimated the thickness of this surface flow region, based on the shear stress and the evaporative flow, to be approximately 0.6 μm at 75% of the radius. As the evaporation rate is almost constant during this stage, the convective velocity at the air–liquid interface is of the order of hundreds of μm/sec. During this stage, Δc is the difference between supersaturation concentration on the periphery and the initial salt concentration on the apex of the drop.

In stage II, nucleation occurs and crystals start to grow near the contact line. This nucleation and subsequent crystal growth are associated with a jet of fluid (Figure 5) (See Movie SM2 Supporting Information). We focus on the growth of the crystal located at the top left region of the droplet (highlighted by the red dashed circle in Figure 5), since the growth of this crystal is the easiest to track, and will consider flows along a radial path through this crystal. However, our discussion is

relevant to all of the formed salt crystals. In the immediate vicinity of the crystal, we expect the concentration to drop from its supersaturated state towards saturation. This reduction in concentration will therefore lead to a reduction in the concentration-based surface tension driving force and hence a lowering of the surface flow (by around 40%). Assuming that the thickness of the surface layer over which this force has an effect is the same as for that in the later part of stage I, this deficit in surface volumetric flow rate requires an outward flow in the lower region of the drop to meet the required evaporative flow (that remains unchanged). During this stage, the droplet height is approximately 15 μm (calculated using the spherical cap approximation). We calculate that the lower layer velocity required to meet this shortfall is around 9 μm/sec. In our experiments, we measure velocities in the jet towards the crystal of around 14 μm/sec. Whilst this is higher than the predicted shortfall, it is of the same order of magnitude and would be consistent with local surface flows in the tangential direction close to the crystal, not considered in our model, that would be directed away from the crystal, increasing the required radial continuity flow.

We also considered both thermal and gravitational effects on the flow. Gravity-driven flow, due to density difference, was disregarded since the droplets size is below the capillary length. Infrared thermography (IRT) was employed in order to elucidate whether the driving mechanism of the observed flow could be a thermocapillary Marangoni effect. The recorded thermal map did not reveal significant temperature gradients during the evaporation process; therefore, we conclude that the jet-like flow is not a result of thermal effects. Infrared thermography (Supporting Information S3) has therefore confirmed previous studies demonstrating that evaporating aqueous droplets do not exhibit thermal Marangoni flow[32,33].

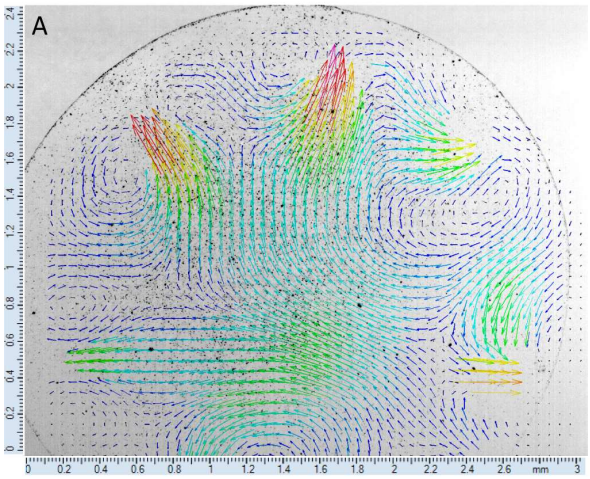
A

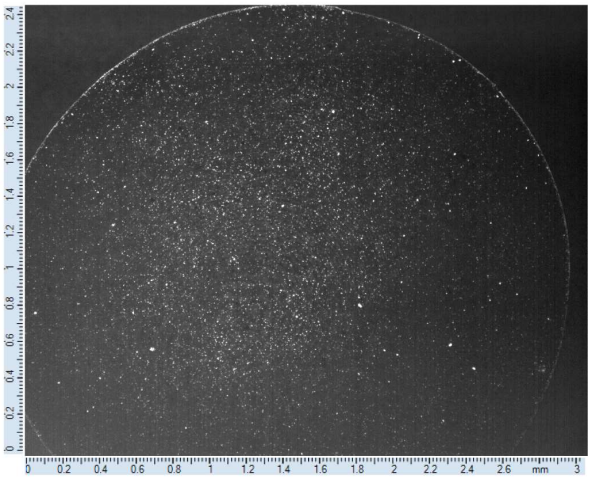

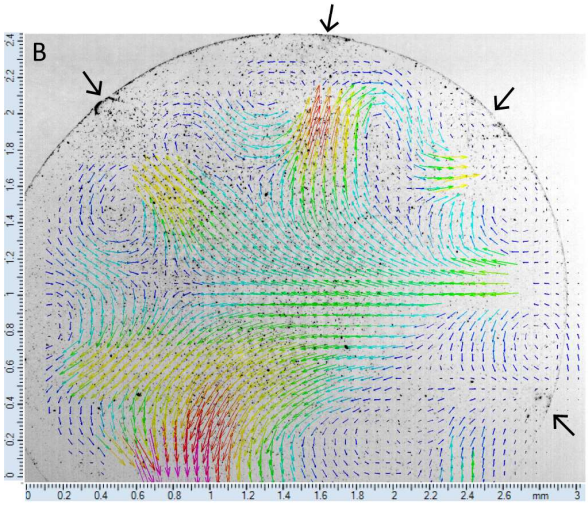
B

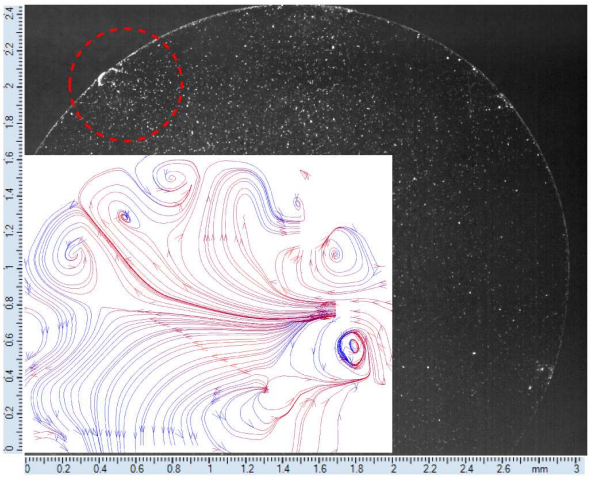

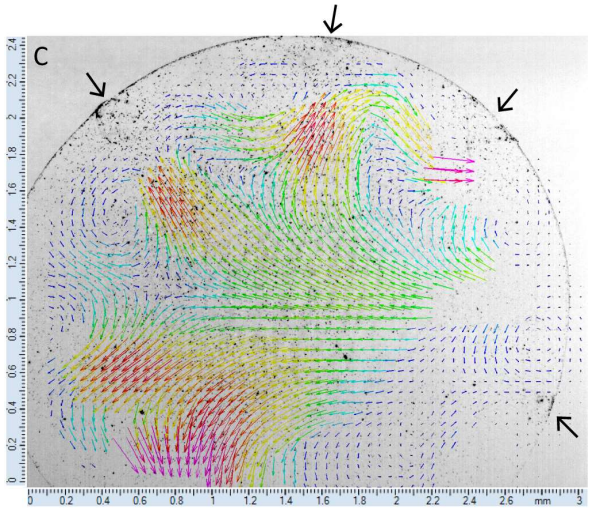
C

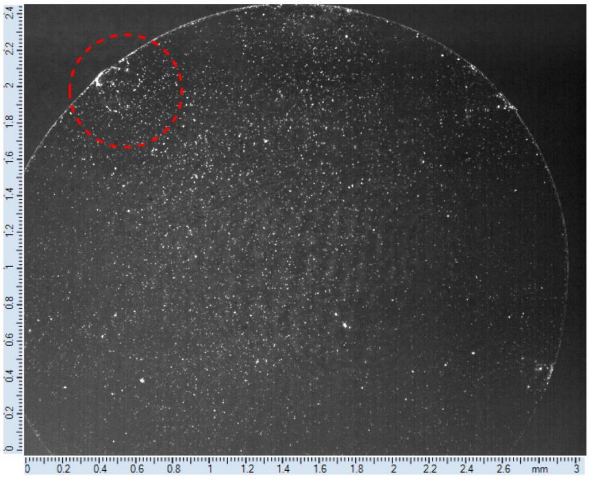

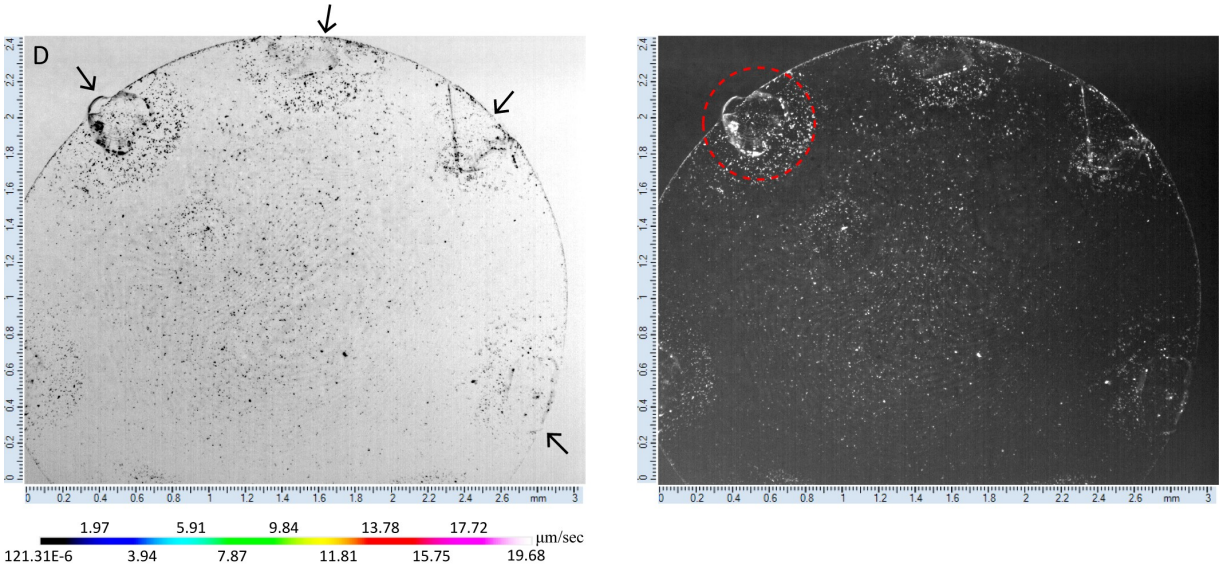

Figure 5: Velocity vectors and micro –PIV images at different times during evaporation. Left: Velocity fields acquired after analysis at different stages of nucleation and crystal growth. Right: micro-PIV images acquired during the experiments illustrating the seeding particles and crystals within the droplet. Inset in right image B shows the flow streamlines for the specific time point. The time frame between images A-B is 21 seconds, and for B-C is seven seconds. D shows the final dried drop.

Whatever the mechanism, the induced jet-like flow entrains surrounding fluid, leading to the formation of two counter-rotating vortices along the base of the drop. Within these vortices, the fluid concentration will be reduced due to salt crystallisation, creating a zone close to a growing crystal where further nucleation is unlikely. This justifies why the deposits form a sequence of crystals around the periphery of the drop rather than a continuous ring. This mechanism contradicts the assumption made in[11] that the crystal spacing is due to the competition between the crystals for ions. It has been found that for the larger droplets (2.7 ± 0.5 µL) the crystals were more evenly spaced, compared to the smaller droplets (1.2 ± 0.2 µL) that were examined here.

The fact that the velocities in the crystallisation stage (Stage II) are significantly higher than those during the initial evaporation, is a clear indication of concentration gradients being greater during this phase. Additionally, during Stage II, vorticity is apparent in the droplet, compared to early and late Stage I with virtually zero vorticity (Figure 6). At the final time of evaporation, liquid cells surround each crystal until the desiccation process is complete. Stage II is of highest importance, illustrating for the first time this jet-like flow of fluid towards the growing crystals that generates vortices on either side of each crystal in an aqueous saline droplet. It is the first time that strong jets of fluid and horizontal vortices are reported within the flow, accompanying the formation of salt crystals, permitting the mechanism of crystal growth to be proposed.

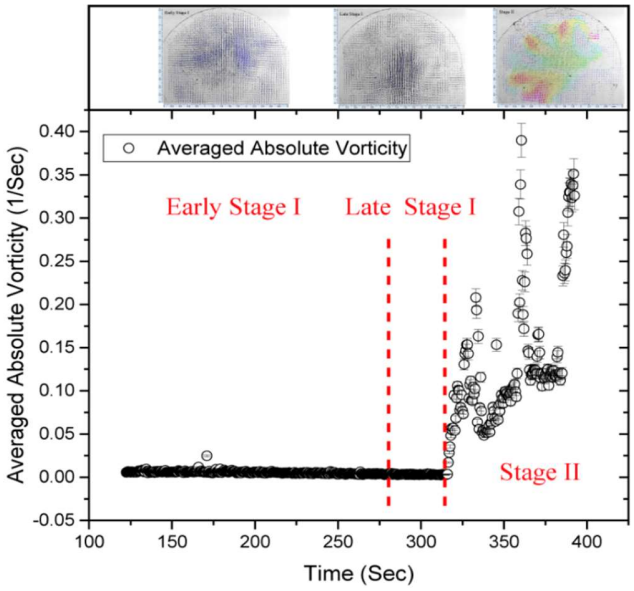

Figure 6: Spatially averaged vorticity as a function of time, during the two stages of evaporation, where Stages I (early and late) and II are the stages described in Figure 1. Stage II is characterised by the appearance of vorticity in the flow, compared to Stage I with virtually zero vorticity. Time t = 0 seconds is the moment of droplet deposition on the substrate.

It is interesting to note that the vorticity changes here are the reverse of what happens with alcohol water mixtures[5], where the concentration differences decrease during evaporation. Here the vorticity appears to be solely dependent on the liquid-solid phase change that occurs due to increase in the salt concentration.

CONCLUSIONS

In conclusion, we report the correlation between flow and crystallisation and the existence of two stages during the evaporation of aqueous saline droplets of relatively high salt concentration on hydrophilic glass slides. The first is a generally outward flow, similar to that observed during pure water evaporation followed by a momentary pause of the flow, where the velocity is reduced by orders of magnitude, possibly because of supersaturation near the contact line. The second, most important stage, reveals that crystal nucleation has a direct effect on the flow regime, leading to increased vorticity, illustrating a crystallisation-driven flow within evaporating aqueous saline droplets. It is worth noting that the same phenomenon is observed for initial contact angles of up to 40^o and for larger droplets (2.7 ± 0.5 μL). Higher initial drop volumes were not examined in this work. Experiments performed with initial contact angles above 40^o reveal a different evaporative behaviour, manifested by depinning and sliding of the contact line on the substrate during evaporation.

ASSOCIATED CONTENT

Supporting Information.

SM1:

Sped up video clip (20 fps), showing the different stages of evaporation during the desiccation of the aqueous saline drops on a hydrophilic glass slide (MP4 video clip).

SM2:

Jet-like flow during the stage of crystal nucleation and growth. During this stage, the velocities developing in the jet are significantly higher compared to these manifested in stage I. The jets are directed towards the growing crystals (MP4 video clip).

S3: The observation of NaCl crystallisation was carried out using passive IR thermography, in order to elucidate whether the driving mechanism of the observed flow could be a thermocapillary Marangoni effect. The IRT experiments did not reveal significant temperature gradients during the evaporation process; therefore, we conclude that the jet-like flow is not a result of thermal effects (PDF).

AUTHOR INFORMATION

Corresponding Author

*E-mail: marina.efstratiou@ed.ac.uk

ORCID

Marina Efstratiou: 0000-0003-4384-1478

Author Contributions

The manuscript was written through contributions of all authors. All authors have given approval to the final version of the manuscript.

ACKNOWLEDGMENT

We would like to acknowledge the Newton Fund, grant number 337066 for the financial support.

ABBREVIATIONS

PIV, Particle Image Velocimetry; IRT, Infrared Thermography

REFERENCES

1. Deegan, R. D.; Bakajin, O.; Dupont, T. F.; Huber, G.; Nagel, S. R.; Witten, T. A. Capillary Flow as the Cause of Ring Stains from Dried Liquid Drops. *Nature* **1997**, *389* (23), 827–829.

2. Xu, X.; Luo, J. Marangoni Flow in an Evaporating Water Droplet. *Appl. Phys. Lett.* **2007**, *91* (124102), 1–4.

3. Semenov, S.; Starov, V. M.; Rubio, R. G.; Agogo, H.; Velarde, M. G. Evaporation of Sessile Water Droplets: Universal Behaviour in Presence of Contact Angle Hysteresis. *Colloids Surfaces A Physicochem. Eng. Asp.* **2011**, *391* (1–3), 135–144.

4. Misyura, S. Y. Evaporation of a Sessile Water Drop and a Drop of Aqueous Salt Solution. *Sci. Rep.* **2017**, No. May, 1–11.

5. Christy, J. R. E.; Hamamoto, Y.; Sefiane, K. Flow Transition within an Evaporating Binary

Mixture Sessile Drop. *Phys. Rev. Lett.* **2011**, *205701* (May), 1–4.

6. Sefiane, K.; David, S.; Shanahan, M. E. R. Wetting and Evaporation of Binary Mixture Drops. *J. Phys. Chem. B* **2008**, *112* (36), 11317–11323.

7. Maki, K. L.; Kumar, S. Fast Evaporation of Spreading Droplets of Colloidal Suspensions. *Langmuir* **2011**, *27* (18), 11347–11363.

8. Liu, W.; Midya, J.; Kappl, M.; Butt, H. J.; Nikoubashman, A. Segregation in Drying Binary Colloidal Droplets. *ACS Nano* **2019**, *13* (5), 4972–4979.

9. Patil, N. D.; Bange, P. G.; Bhardwaj, R.; Sharma, A. Effects of Substrate Heating and Wettability on Evaporation Dynamics and Deposition Patterns for a Sessile Water Droplet Containing Colloidal Particles. *Langmuir* **2016**, *32* (45), 11958–11972.

10. Sung, P. F.; Wang, L.; Harris, M. T. Deposition of Colloidal Particles during the Evaporation of Sessile Drops: Dilute Colloidal Dispersions. *Int. J. Chem. Eng.* **2019**, *2019*, 1–12.

11. Takhistov, P.; Chang, H. Complex Stain Morphologies. *Ind. Eng. Chem. Res* **2002**, *41*, 6256–6269.

12. Kaya, D.; Belyi, V. A.; Muthukumar, M. Pattern Formation in Drying Droplets of Polyelectrolyte and Salt. *J. Chem. Phys.* **2010**, *133* (114905), 1–9.

13. Choudhury, M. D.; Dutta, T.; Tarafdar, S. Pattern Formation in Droplets of Starch Gels Containing NaCl Dried on Different Surfaces. *Colloids Surfaces A Physicochem. Eng. Asp.* **2013**, *432*, 110–118.

14. Kuznetsov, G. V.; Feoktistov, D. V.; Orlova, E. G.; Misyura, S. Y.; Morozov, V. S.; Islamova, a. G. Evaporation Modes of LiBr, CaCl2, LiCl, NaCl Aqueous Salt Solution Droplets on Aluminum Surface. *Int. J. Heat Mass Transf.* **2018**, *126*, 161–168.

15. Lee, S. J.; Hong, J.; Choi, Y. S. Evaporation-Induced Flows inside a Confined Droplet of Diluted Saline Solution. *Langmuir* **2014**, *30* (26), 7710–7715.

16. Misyura, S. Y. Evaporation and Heat and Mass Transfer of a Sessile Drop of Aqueous Salt Solution on Heated Wall. *Int. J. Heat Mass Transf.* **2018**, *116*, 667–674.

17. Ponomarev, K. O.; Feoktistov, D. V.; Marchuk, I. V. Evaporation Rate of Aqueous Salt Solutions Droplets. *MATEC Web Conf.* **2016**, *91* (01029), 1–4.

18. Vázquez, P.; Thomachot-Schneider, C.; Mouhoubi, K.; Fronteau, G.; Gommeaux, M.; Benavente, D.; Barbin, V.; Bodnar, J. L. Infrared Thermography Monitoring of the NaCl Crystallisation Process. *Infrared Phys. Technol.* **2015**, *71*, 198–207.

19. Zhang, J.; Borg, M. K.; Sefiane, K.; Reese, J. M. Wetting and Evaporation of Salt-Water Nanodroplets: A Molecular Dynamics Investigation. *Phys. Rev. E - Stat. Nonlinear, Soft Matter Phys.* **2015**, *92* (5), 1–11.

20. Quilaqueo, M.; Aguilera, J. M. Crystallization of NaCl by Fast Evaporation of Water in Droplets of NaCl Solutions. *FRIN* **2016**, *84*, 143–149.

21. Sghaier, N.; Prat, M.; Nasrallah, S. Ben. On the Influence of Sodium Chloride Concentration on Equilibrium Contact Angle. *Chem. Eng. J.* **2006**, *122*, 47–53.

22. Zhong, X.; Ren, J.; Duan, F. Wettability Effect on Evaporation Dynamics and Crystalline

Patterns of Sessile Saline Droplets. *J. Phys. Chem. B* **2017**, *121* (33), 7924–7933.

23. Kuznetsov, G. V; Feoktistov, D. V; Orlova, E. G.; Misyura, S. Y.; Morozov, V. S.; Islamova, A. G. International Journal of Heat and Mass Transfer Evaporation Modes of LiBr , CaCl 2 , LiCl , NaCl Aqueous Salt Solution Droplets on Aluminum Surface. *Int. J. Heat Mass Transf.* **2018**, *126*, 161–168.

24. Ponomarev, O, K.; Feoktistov, V, D.; Marchuk, V, I. EVAPORATION RATE OF AQUEOUS SALT. *MATEC Web Conf.* **2017**, *01029*, 1–4.

25. Kang, K. H.; Lim, H. C.; Lee, H. W.; Lee, S. J. Evaporation-Induced Saline Rayleigh Convection inside a Colloidal Droplet. *Phys. Fluids* **2013**, *25* (4), 1–21.

26. Soulié, V.; Karpitschka, S.; Lequien, F.; Prené, P.; Zemb, T.; Moehwald, H.; Riegler, H. The Evaporation Behavior of Sessile Droplets from Aqueous Saline Solutions. *Phys. Chem. Chem. Phys.* **2015**, *17* (34), 22296–22303.

27. Marin, A.; Karpitschka, S.; Noguera-marín, D.; Cabrerizo-vílchez, M. A.; Rossi, M.; Kähler, C. J.; Valverde, M. A. R. Solutal Marangoni Flow as the Cause of Ring Stains from Drying Salty Colloidal Drops. *Phys. Rev. Fluids* **2019**, *4* (4), 41601.

28. Shahidzadeh-Bonn, N.; Rafai, S.; Bonn, D.; Wegdam, G. Salt Crystallization during Evaporation: Impact of Interfacial Properties. *Langmuir* **2008**, *24* (16), 8599–8605.

29. Mcbride, S. A.; Dash, S.; Varanasi, K. K. Evaporative Crystallization in Drops on Superhydrophobic and Liquid-Impregnated Surfaces. *Langmuir* **2018**, *34*, 12350–12358.

30. Shahidzadeh, N.; Schut, M. F. L.; Desarnaud, J.; Prat, M.; Bonn, D. Salt Stains from

Evaporating Droplets. *Sci. Rep.* **2015**, *5*, 1–9.

31. Desarnaud, J.; Derluyn, H.; Carmeliet, J.; Bonn, D.; Shahidzadeh, N. Metastability Limit for the Nucleation of NaCl Crystals in Confinement. *J. Phys. Chem. Lett.* **2014**, *5* (5), 890–895.

32. Sefiane, K.; Moffat, J, R.; Matar, O. .; Craster, R. . Self-Excited Hydrothermal Waves in Evaporating Sessile Drops. *Appl. Phys. Lett.* **2016**, *074103* (August 2008), 91–94.

33. Hu, H.; Larson, R. G. Marangoni Effect Reverses Coffee-Ring Depositions. *J. Phys. Chem. B* **2006**, *110* (14), 7090–7094.

34. Desarnaud, J.; Derluyn, H.; Carmeliet, J.; Bonn, D.; Shahidzadeh, N. Metastability Limit for the Nucleation of NaCl Crystals in Confinement. *J. Phys. Chem. Lett.* **2014**, *5* (5), 890–895.

TOC GRAPHICS